



Effects of Line Energy on Microstructure and Mechanical Properties of CoCrFeNiBSi High-Entropy Alloy Laser Cladding Coatings

Fengyuan Shu¹ · Bin Wang¹ · Hongyun Zhao¹ · Caiwang Tan¹ · Jialiang Zhou¹ · Jian Zhang²

Submitted: 6 November 2019 / in revised form: 13 February 2020 / Published online: 28 February 2020
© ASM International 2020

Abstract Amorphous alloys possess excellent mechanical properties such as high hardness and high wear resistance. CoCrFeNiBSi high-entropy alloys with amorphous phase have been prepared on the surface of H13 steel by utilizing various laser line energies. The microstructure, phase, hardness, and wear resistance of the cladding coatings were studied. The glass-forming ability of different cladding coatings was compared by observing the change on the dilution rate. The results show that the coatings consisted of an amorphous phase and a crystallization phase, which contained FeNi₃, α -Co, and Cr₂C. As the laser line energy was increased, the dilution rate of the coatings increased and the content of the amorphous phase decreased. Coatings with high content of amorphous phase showed satisfied hardness and wear resistance.

Keywords amorphous phase · high-entropy alloy · high-temperature wear resistance · laser cladding

Introduction

H13 steel is preferentially employed in the design of hot working die due to its excellent hardenability and hot cracking resistance (Ref 1–3). The die steel suffers from friction and surface damage in the process of forging or die casting, which limits its long-term use and reduces its production efficiency (Ref 4, 5). Hence, there is an urgent demand for H13 steel to possess exceptional wear resistance. Amorphous alloys, also known as metallic glasses, have recently received extensive attention. As a result of their high microhardness (Ref 6) and desirable wear resistance (Ref 7), they are suitable for deposition on the surface of H13, thereby improving its service life.

High-entropy alloys (HEA) possess strong glass-formation ability (GFA) which enables them to easily form an amorphous microstructure (Ref 8–10). Zhao et al. (Ref 11) reported that the Zr₂₀Ti₂₀Cu₂₀Ni₂₀Be₂₀ (HEA) prepared by arc-melting was mainly composed of amorphous structure and its high hardness promoted an outstanding wear resistance. Therefore, the amorphous coatings of HEA could be more durable in a harsh service environment.

To date, many studies have investigated the preparation of HEA coatings, including plasma cladding (Ref 12), magnetron sputtering (Ref 13) plasma spraying (Ref 14), and laser cladding (Ref 15, 16). Compared with other methods, laser cladding shows obvious advantages, including metallurgical bonding between coatings and substrate as well as rapid melting and cooling processes. Jiang et al. (Ref 17) investigated the wear behavior of laser-cladded CoFeNi₂V_{0.5}Nb_{0.75} and CoFeNi₂V_{0.5}Nb HEA coatings. Their results showed that the coatings possessed better wear resistance and the wear mass loss of the coatings was one-third of that of 304 stainless steel substrates. Wu et al. (Ref 18) revealed that the

✉ Caiwang Tan
755741983@qq.com

✉ Jian Zhang
zhangjianwenzhou@qq.com

¹ State Key Laboratory of Advanced Welding and Joining at Weihai, Shandong Provincial Key Laboratory of Special Welding Technology, Harbin Institute of Technology, Weihai 264209, China

² Zhejiang Provincial Key Laboratory of Laser Processing Robot, Wenzhou University, Wenzhou 325035, Zhejiang, China

microhardness value of FeCoCrAlCuNi_{0.5} HEA coatings fabricated by laser cladding could reach 636 HV, which was at least 6.6 times that of the substrate. Jiang et al. (Ref 19) demonstrated that the AlCoCr_xFeNi HEA coatings could be successfully fabricated on 45# steel by the laser-cladding technique. The HEA coatings with $x = 1.5$ exhibited prominent corrosion resistance with higher corrosion potential and broader and lower passive current.

Laser cladding is characterized by a high cooling rate of 10^6 K/s, making it a promising approach to meet the requirements of amorphous phase formation. Nevertheless, few researchers have studied the amorphous phase generated in HEA coatings fabricated by laser cladding and the high-temperature wear resistance of such coatings. Thus, in the present work, the CoCrFeNiBSi HEA coatings were prepared on H13 steel surface with different laser line energies. The changes of amorphous content in the microstructure and the difference in hardness and high-temperature wear resistance under various process parameters were observed, and the reasons for the intriguing results were revealed by the cooling and dilution rates. It is hoped that the present paper might be helpful for the study of GFA.

Experimental Procedures

Materials and Methods

H13 steel plate with the dimensions of 200 mm × 100 mm × 20 mm was used as substrate during the laser cladding process. The starting powders were powdery mixtures of all elements. They were mixed and milled utilizing a planetary ball milling machine to ensure the uniformity of powders. The particle size of the cladded powders was 200 to 400 mesh, and the cladded powders were preplaced on the substrate with a thickness of 200 μm before laser cladding. Table 1 presents the chemical composition of the substrate and the cladded powders. The workpiece was protected in an argon chamber.

In this experiment, cladded coatings with 50% overlap were fabricated using an RH-700 Nd:YAG solid-state laser beam generator (Hebei Ruichi Weiye Technology Co., Ltd) connected to a mobile control system for numerical control. To optimize the laser-cladding process parameters,

electric current, pulse width, laser scanning velocity, defocus amount, and beam diameter were selected to be 380 A, 8 ms, 100 mm/min, 20 mm, and 2.2 mm to 2.5 mm, respectively. The laser line energies used to study the effects on the microstructure and mechanical properties of the cladding coatings were 140 J/mm, 210 J/mm, 280 J/mm, and 420 J/mm.

Microstructural Examination

The cross-sections of coatings with different laser line energies were detected by metallographic microscopy (MM). The microstructures of the coatings were analyzed by scanning electron microscopy (SEM) and x-ray diffraction (XRD) analysis. The amorphous phase was identified by transmission electron microscopy (TEM). The wear morphology and elemental content of wear debris of coatings were observed by SEM and energy dispersive x-ray spectroscopy (EDS).

Wear Testing

The microhardness was tested along the depth direction of the cladded coatings with a TH701-type Vickers indenter under a load of 1000 g and a duration of 15 s. To evaluate the high-temperature wear resistance of the HEA amorphous coatings, the wear test was performed using a high-temperature ball-on-disc-type friction and a wear testing machine (HT-1000). Zirconia ceramic balls (diameter of 5 mm) were selected as the counterpart material. The tested surface got previously grounded using 400-grit SiC papers and cut into samples with dimensions of 20 mm × 20 mm × 7 mm. The experimental conditions were: 500 °C, 1150 g load, 1 h sliding time, 3 mm rotational radius, and 1120 rotations per minute.

Calculation of Dilution Rate

Dilution rate was one of the important indicators to evaluate the results of laser cladding. The dilution rate was calculated as follows:

$$\eta = \frac{H - h}{H},$$

Table 1 Chemical composition of substrate and HAE powders

| Element | C | Si | Mn | Cr | Mo | V | S | P | Fe | Co | Ni | B |
|-----------------|-----------|-----------|-----------|-----------|-----------|-----------|------|------|------|-----|-----|-----|
| H13 steel, wt.% | 0.32–0.45 | 0.80–1.20 | 0.20–0.50 | 4.75–5.50 | 1.10–1.75 | 0.80–1.20 | 0.03 | 0.03 | Bal. | ... | ... | ... |
| Powders, at.% | ... | 7 | ... | 29 | ... | ... | ... | ... | 8 | 34 | 8 | 14 |

where η , H , and h are the dilution rate, total height of coatings, and height above the substrate, respectively.

Results and Discussion

Microstructure Analysis

The different regions of cross-sections were investigated by SEM analysis. Figure 1 shows the micromorphology of the upper region of the cladded coatings obtained with different laser line energies. The microstructure of the upper region was a mixture of amorphous and some crystalline phases, which is well consistent with previous research (Ref 20, 21). The light-color areas indicate the amorphous phases without grain boundary, while the bulk crystallized phase is represented in dark color. It can be seen from the micromorphology of the upper layer of different coatings that the proportion of the amorphous phase decreased when the laser line energy increased from 140 J/mm to 420 J/

mm. The increased laser line energy elevated the heat input, the maximum temperature in the thermal cycle, and the heat-affected zone (HAZ) of the substrate. Consequently, the cooling rate during the solidification of the liquid metal slowed down and failed to meet the conditions under which the amorphous phase can be formed, leading to a long-range disorder arrangement of atoms. As a result, the formation of the amorphous and crystallization phases was inhibited and promoted, respectively.

Figure 2 illustrates the microstructure of the bottom regions of the coatings obtained with different laser line energies. As one of the obvious advantages of laser cladding, metallurgical bonding between coatings and substrates was achieved. The bottom regions of cladding coatings were dominated by the columnar phase, and the proportion of columnar dendrites increased with the increase of laser line energy. Full columnar dendrites at the bottom regions of the cladding coatings were observed when the laser line energy reached 420 J/mm, as shown in Fig. 2(d). The reason why the proportion of columnar dendrites differed was associated with the amount of

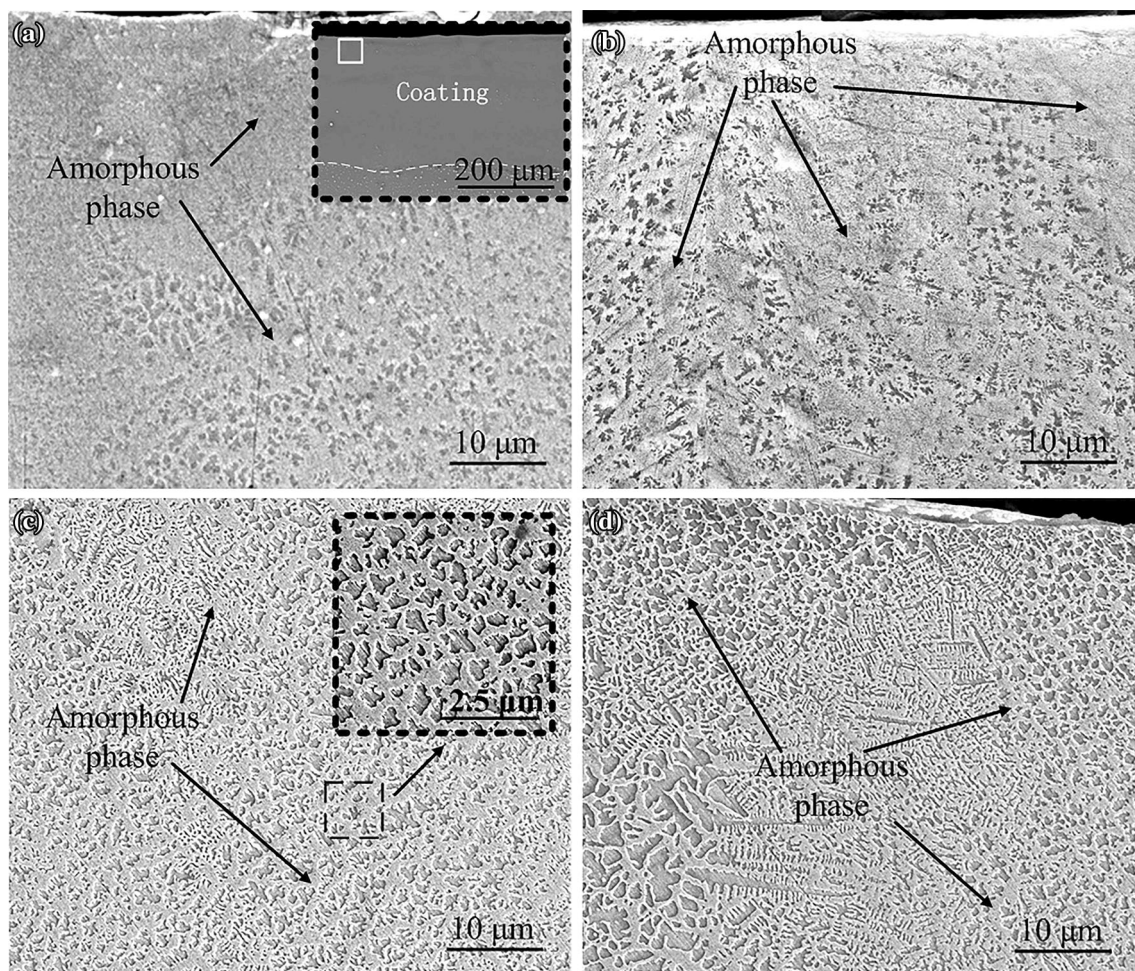


Fig. 1 Upper region of different cladded coatings: (a) 140 J/mm, (b) 210 J/mm, (c) 280 J/mm, and (d) 420 J/mm

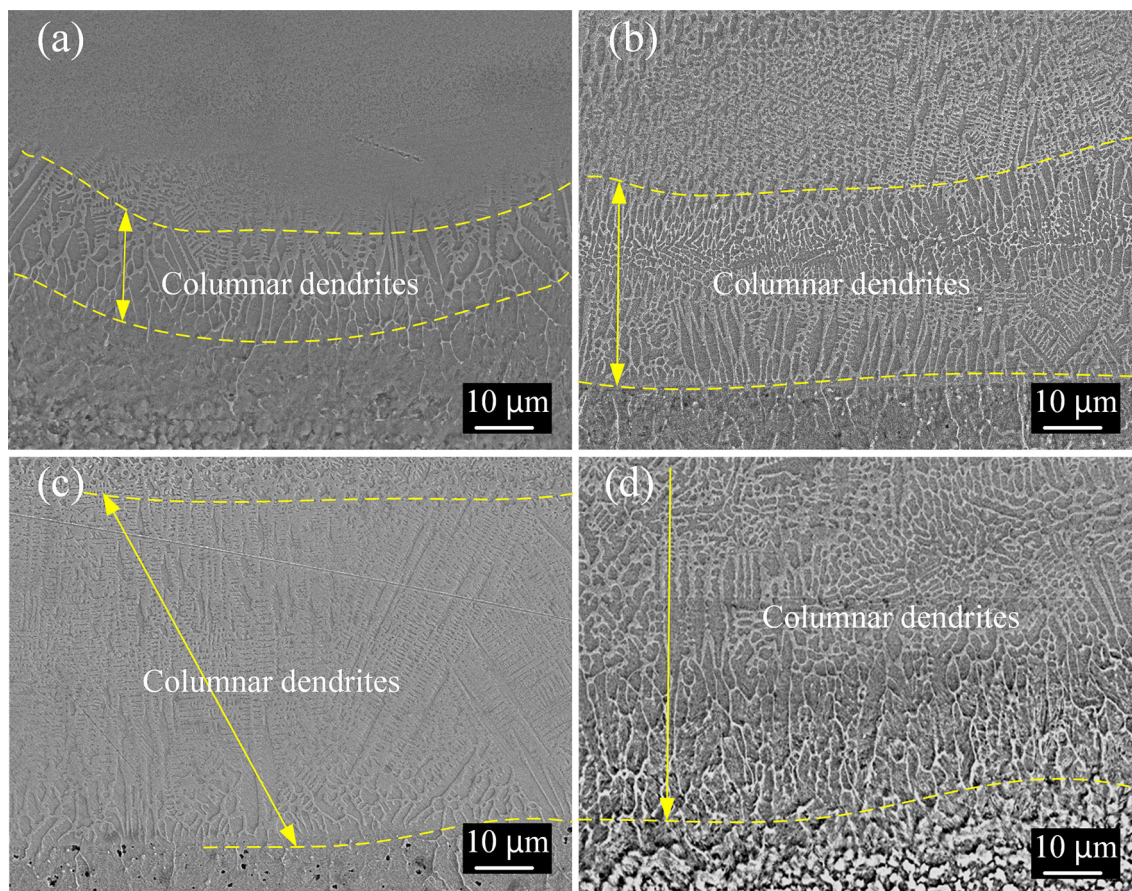


Fig. 2 Bottom region of different cladded coatings: (a) 140 J/mm, (b) 210 J/mm, (c) 280 J/mm, and (d) 420 J/mm

irradiation energy received in the molten pool. With the increase of laser energy, the residence time of the molten pool metals during the high-temperature phase became longer and the solidification rate decreased. Hence the grains had adequate time to nucleate and grow, resulting in the greater production of coarser columnar crystals. It can also be appreciated from Fig. 2 that columnar crystals grew perpendicularly to the fusion line toward the top of the cladding coatings, the direction with the greatest temperature gradient.

The XRD patterns were used to detect the phase of the amorphous coatings with different laser line energies, as indicated by Fig. 3. An obvious broaden peak can be appreciated in the 2θ region of 44° , as shown in Fig. 3(a). The presence of the amorphous phase in the coatings is responsible for the phenomenon of diffraction peak broadening. Furthermore, a few sharp crystal peaks can be appreciated in the XRD patterns as well, demonstrating the existence of a mixture of amorphous and crystalline phases in the deposited Co-based alloy amorphous coatings. The crystalline phases were composed of FeNi_3 , $\alpha\text{-Co}$, and Cr_2C . Figure 3(b) shows the width of the broaden peak decreasing with the increase of the laser line energy. It was

confirmed that the increase of laser line energy led to the decrease of amorphous content, which was consistent with the SEM analysis observation. Note that only the diffraction peaks in the 2θ region of 44° are slightly shifted in the diffraction patterns obtained with different laser line energies. Therefore, the lattice constant change was not caused by the doped atoms but was probably the reflection of the lattice distortion due to the macroresidual stress, which may have caused anisotropic shrinkage of the lattice and changes in the interplanar spacing (Ref 22). Consequently, a shift of peaks appeared in the XRD results, but this would not affect the subsequent analysis.

The existence of the amorphous phase in the Co-based alloy cladding coatings was corroborated by using TEM. Figure 4 shows the bright-field image (BM) and selected-area electron diffraction (SAED) of the upper layer. Figure 4(b) shows the SAED test result of selected area *B* in Fig. 4(a). Since the atoms in the amorphous phase were arranged in long-range disorder, their diffraction spots would not emerge periodic potential field. Note that three dispersive diffraction rings appear in the SAED pattern, but this does not guarantee the presence of three correspondent broad diffraction peaks in the XRD pattern given that this

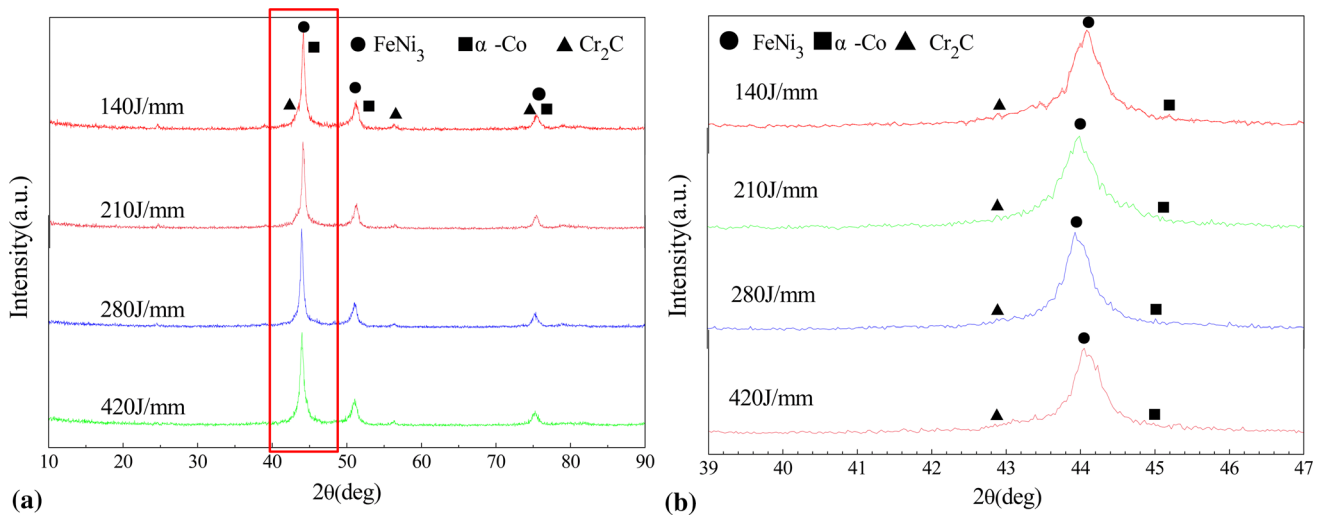


Fig. 3 (a) XRD profile of amorphous coatings with different laser line energies; (b) enlarged view of red area in Fig. 3(a)

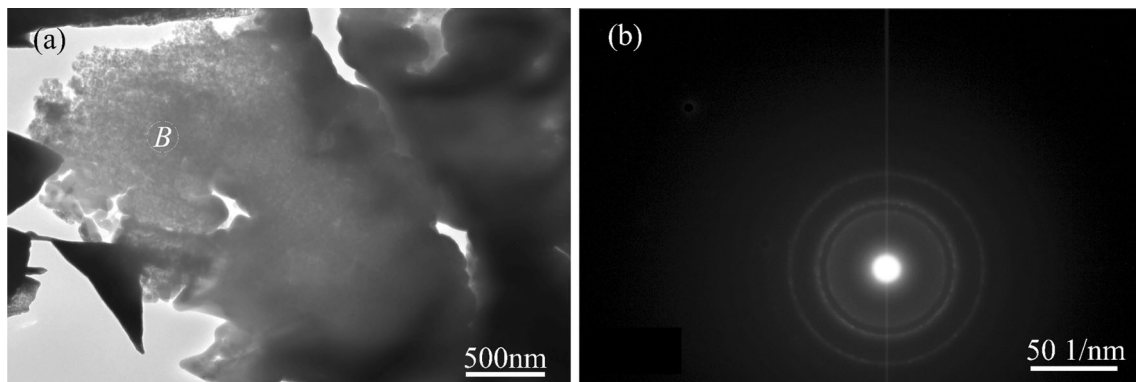


Fig. 4 TEM images: (a) bright-field image and (b) selected-area electron diffraction of area *B* in (a)

region in the upper layer is not a complete amorphous phase one but a mixture composed of amorphous and crystalline phases. Therefore, the other two diffraction rings of polycrystalline phase should correspond to the sharp diffraction peak in XRD. The polycrystalline was probably FeNi₃ with the family of crystal planes (110) and (111) (PDF #88-1715).

Microhardness Analysis

Figure 5 shows the microhardness profiles along the depth of coatings with different laser line energies. On the one hand, the microhardness of the coatings is significantly higher than that of the substrate for each curve, and the average value exceeds 1000 HV. On the other, the microhardness of the cladding coatings appears as a descending trend with the increase of laser line energy. This phenomenon can be explained by the microhardness of the crystallized phase’s being lower than that of the amorphous phase (Ref 23). When excessive laser energy was absorbed

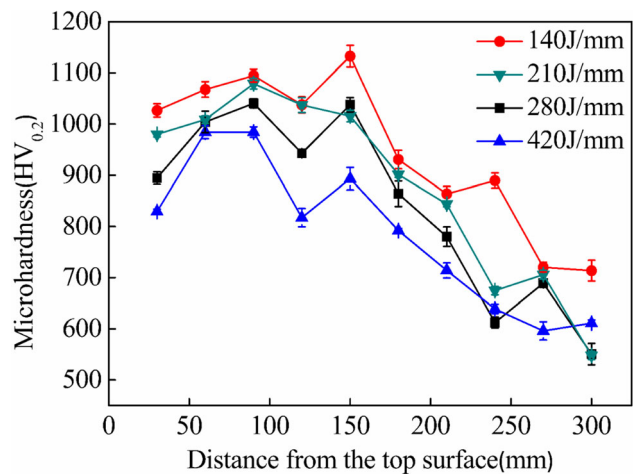


Fig. 5 Microhardness profiles along depth of coatings with different line energies

into the molten pool, the content of the amorphous phase decreased, as analyzed above, resulting in the impair of hardness of coatings.

The distribution of the crystalline phase affected the stability of microhardness testing. More amorphous phase and less crystalline phase were present in the upper regions. However, in the middle of the cladding coatings, with a range of 100 μm to 150 μm from the top layer, the microhardness fluctuated with an amplitude of 200 HV approximately, which was attributed to the content of the crystallized phase increasing as the distance from the top layer increased, causing the area of crystallization phase to be pressed easily by the indenter. The microhardness curve presents a significant descending trend as the distance gets over 150 μm . The increase of the crystalline phase content weakened the microhardness of the bottom layer.

High-Temperature Wear Properties

Figure 6 shows the test results of high-temperature wear behavior. Figure 6(a) illustrates the curves of various friction coefficients along time during the 1-h friction wear test of cladding coatings with different line energies. When the value got above 210 J/mm, the friction coefficient of the cladding coatings increased with the increase of laser line energy. The wear mass loss of coatings and laser line energy increased simultaneously, as shown in Fig. 6(b). As mentioned above, since the decrease of the amorphous phase content would lead to the reduction of microhardness, the adhesive wear between the coatings and grinding material would aggravate, resulting in the increase of the friction coefficient and the impair of the wear resistance. An engaging phenomenon observed was that the friction coefficient of the cladding coatings with a laser line energy of 140 J/mm was higher than that of the coatings obtained at 210 J/mm. When the amorphous phase content reached a certain level, the tendency of brittle cracking increased, which tended to enhance the chimeric effect between the

coatings and the abrasive material, thus further improving the friction coefficient of the coatings.

Figure 7 shows the micromorphologies of the worn surface obtained with different laser line energies. It can be detected from the morphologies that the high-temperature wear mechanism of the cladding coatings was mainly abrasive wear and oxidation wear. The worn surface morphology of the upper layer was smooth and exhibited slight plowing grooves with little oxidation patches, as shown in Fig. 7(a) and (b). However, the cracks appeared when the coating was subject to a laser line energy of 140 J/mm, which confirms the above analysis on the increase of friction coefficient. When the line energy approached 280 J/mm, a large number of plowing grooves were produced on the upper layer together with sparsely distributed oxidized areas, as shown in Fig. 7(c). The large areas of oxidation patches were formed after friction and wear as line energy was up to 420 J/mm, as indicated by Fig. 7(d). The decrease of the amorphous phase content created plowing grooves and large areas of oxidation patches. Obviously, the high hardness of the amorphous phase contributed to the wear resistance of the coatings.

Calculation Results of Dilution Rate

The dilution effect of the H13 steel was able to change the chemical composition in the molten pool, thereby affecting the microstructure and properties of the cladding coatings. Figure 8 shows the cross-sections of the coatings obtained with different line energies. According to the size of the coatings measured in Fig. 8, the molten depth increased as the laser line energy increased, and as a result, the calculated dilution rate of the coatings increased, as shown by Fig. 9. When the HEA coatings were subject to the dilution effect, the atomic exchange between substrate and coatings

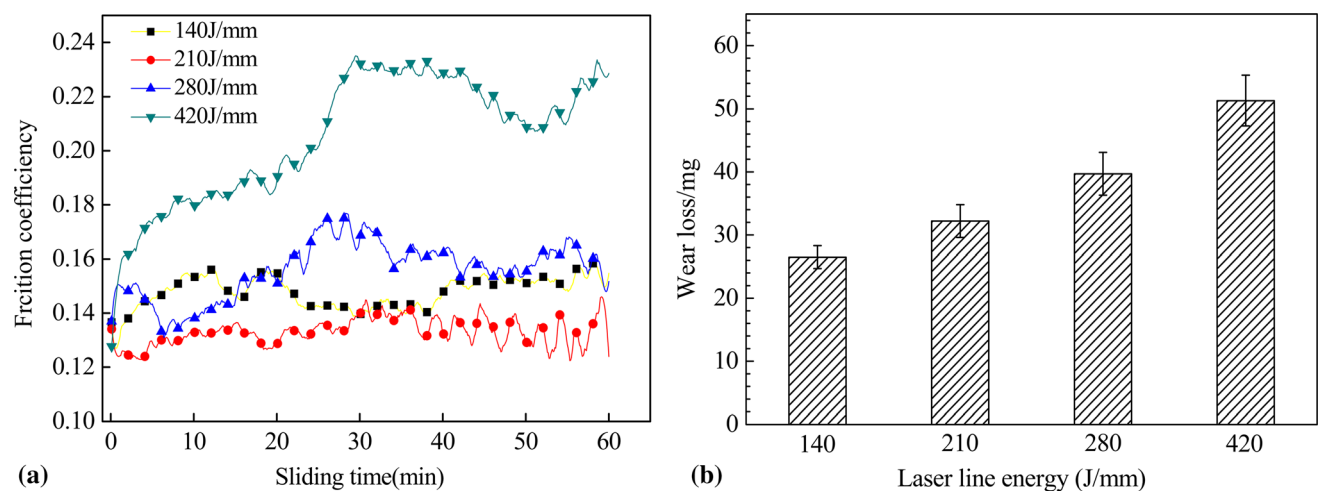


Fig. 6 (a) Friction coefficient–time curve of friction and wear, and (b) wear mass of upper layers with same load at different laser line energies

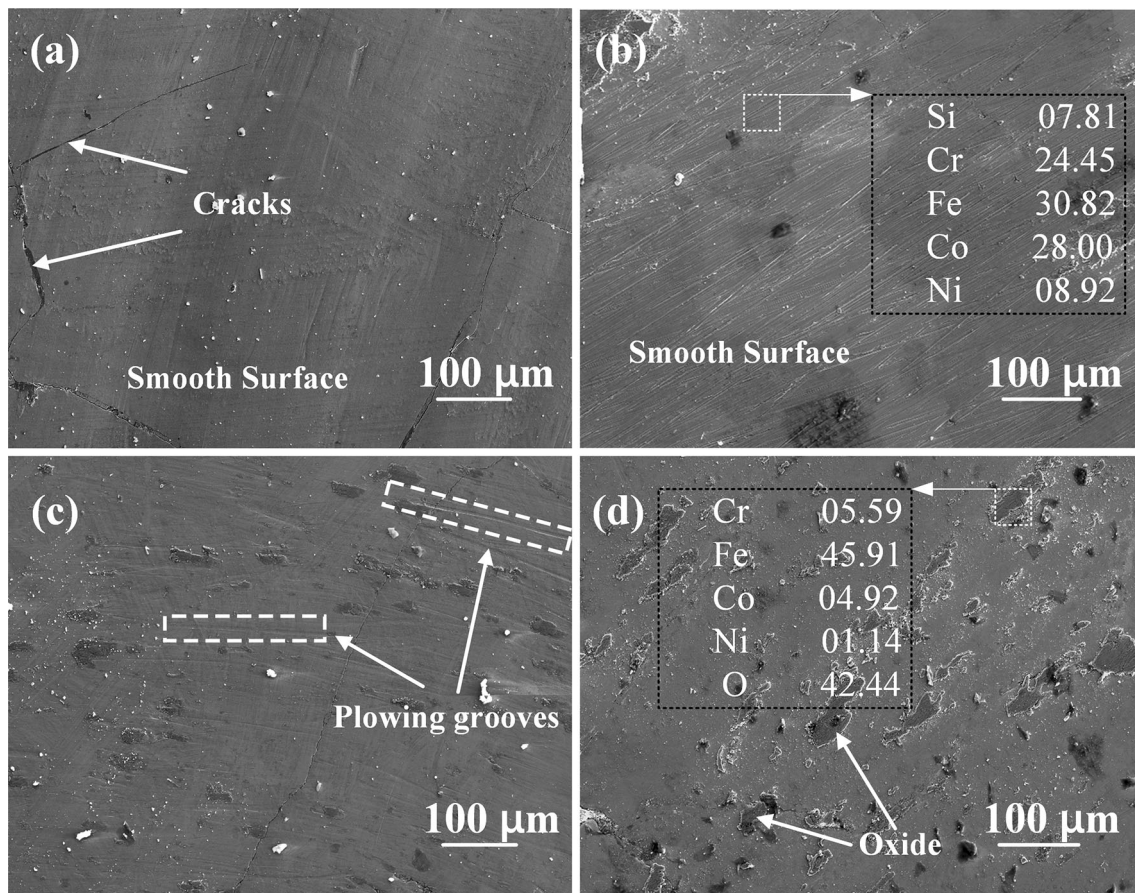


Fig. 7 Micromorphologies of worn surfaces: (a) 140 J/mm, (b) 210 J/mm, (c) 280 J/mm, and (d) 420 J/mm

occurred and the chemical composition of the bottom layer changed. At that time, the concentration fluctuation promoted the formation of columnar dendrites in this region, as shown in Fig. 2.

The bonding strength between the coatings and substrate was weak when the dilution rate was low. When the high dilution rate arose, the substrate material had a significant adverse effect on the properties of the coatings. Controlling the dilution rate within a certain range was beneficial to guarantee a limited influence of the substrate upon the properties of the coatings and a qualified bonding strength between the coatings and the substrate simultaneously. Dilution rates of 24.24% and 24.36% were obtained when the laser line energy was 140 J/mm and 210 J/mm, respectively, and meanwhile, they exhibited desired mechanical properties, as the results show.

Discussion

It has been acknowledged that cladding materials with denser atomic packing (Ref 24) and higher entropy of mixing (Ref 25) should possess better GFA. Yan et al.

(Ref 26) paid attention to the atomic radius influencing GFA significantly through directly affecting the stacking density of ordered atomic clusters in the liquid alloy. They proposed the glass forming ability index λ_n based on the above theory, and the maximum amorphous content was obtained when the index was 0.18. According to our previous research, the lesser the content of Fe diffused into the cladding coatings due to dilution, the closer the value of λ_n to 0.18, therefore the more amorphous content obtained (Ref 27). That was because the content of Fe element played a dominating role in grading the GFA of the clad materials. Compared with other elements, Fe element showed a stronger diffusion ability and its content varied dramatically at the bottom layer of the coatings (Ref 28). This is in good agreement with the results shown in Fig. 2. The Fe element from the substrate entered the bottom region of the coatings, and the concentration fluctuation created the conditions for the formation of columnar dendrites. With the increase of dilution rate, the content of Fe diffused into the cladding coatings increased, and nucleation and growth of substantial columnar crystals occurred at the bottom layer. Thus, the areas occupied by amorphous phase decreased, reflecting the weakening of GFA.

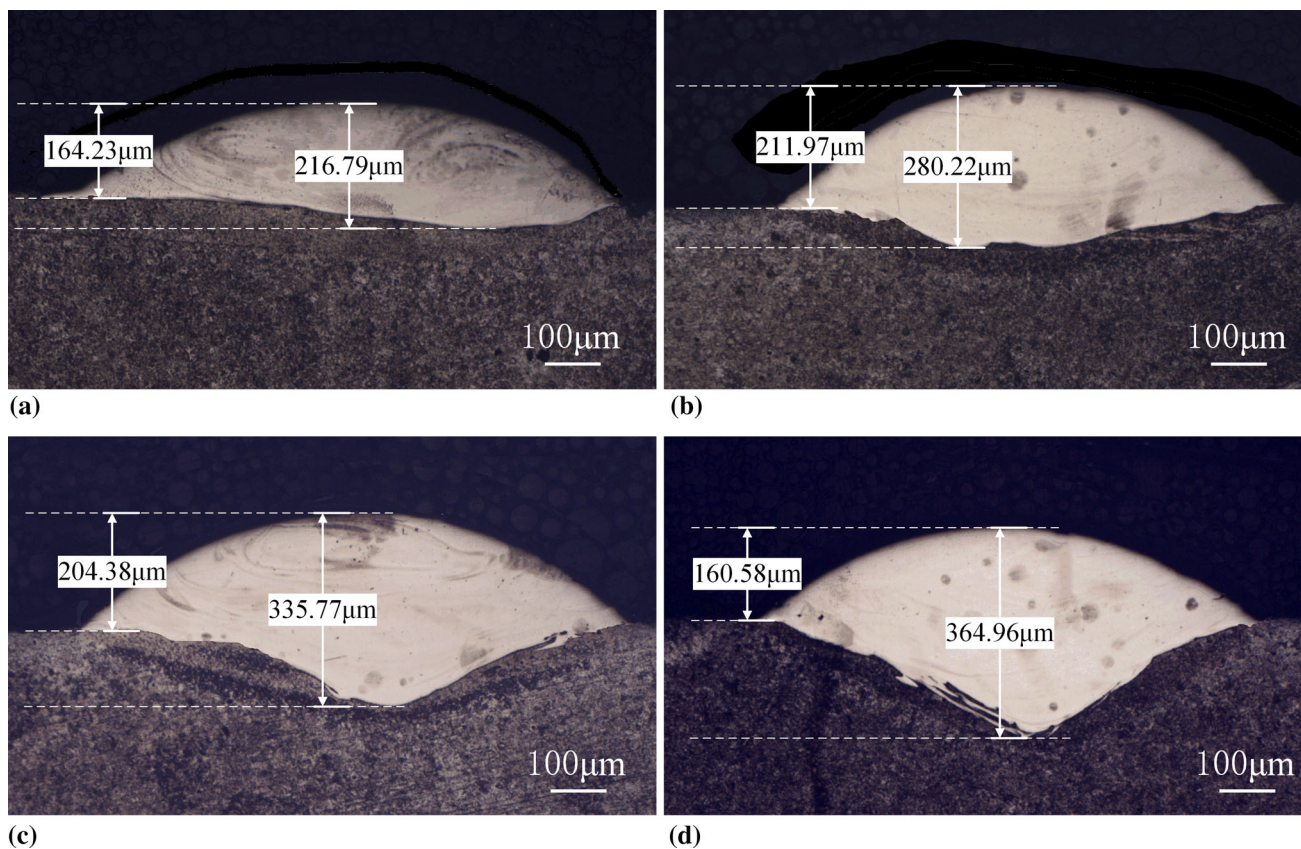


Fig. 8 Cross-section of coatings with different line energies: (a) 140 J/mm, (b) 210 J/mm, (c) 280 J/mm, and (d) 420 J/mm

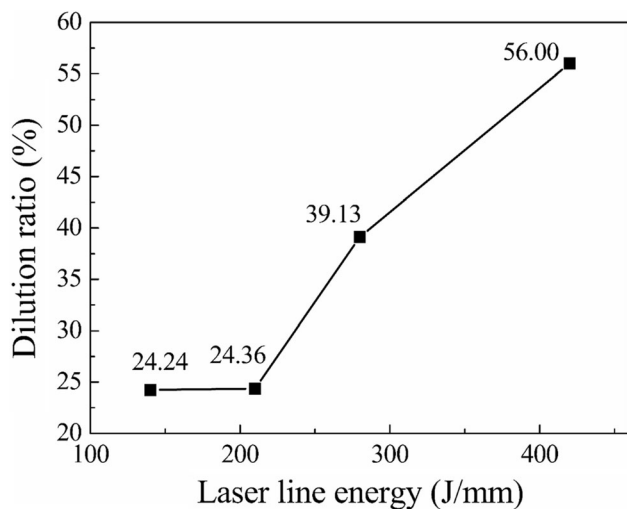


Fig. 9 Dilution rates of coatings with different line energies

Conclusions

1. Amorphous coatings were successfully fabricated by laser cladding CoCrFeNiBSi high-entropy alloy on H13 steel substrate.
2. The laser line energy affected the amorphous phase content in the coatings. When the laser line energy

increased, the cooling rate as well as the amorphous phase content of the coatings decreased simultaneously, and the number of crystallized phases increased. The crystallization phases included FeNi_3 , $\alpha\text{-Co}$, and Cr_2C .

3. As the laser line energy was increased, the dilution rate by the substrate increased, which led to deterioration of the glass forming ability of the coatings, thereby creating a reduction of the amorphous phase content and an increase of columnar dendrites in the covering area.
4. Although no obvious differences were found in the worn surfaces by abrasive wear, reduced amorphous phase content in the coatings resulted in lower microhardness, more wear mass loss, and more severe oxidation wear, which was mainly responsible for the deteriorated wear resistance.

Acknowledgments This study was supported by National Natural Science Foundation of China (Grant No. 51905126), State Key Lab of Advanced Welding and Joining, Harbin Institute of Technology, the China Postdoctoral Science Foundation-General Program (Grant No. 2018M641822), and National Natural Science Foundation of China (General Program, Grant No. 51875129).

References

- J. Zhu, Z. Zhang, and J. Xie, Improving Strength and Ductility of H13 Die Steel by Pre-tempering Treatment and Its Mechanism, *Mater. Sci. Eng. A*, 2019, **752**, p 101-114
- M. Pérez and F.J. Belzunce, A Comparative Study of Salt-Bath Nitrocarburizing and Gas Nitriding Followed by Post-oxidation Used as Surface Treatments of H13 Hot Forging Dies, *Surf. Coat. Technol.*, 2016, **305**, p 146-157
- J. Marashi, E. Yakushina, P. Xirouchakis, R. Zante, and J. Foster, An Evaluation of H13 Tool Steel Deformation in Hot Forging Conditions, *J. Mater. Process. Technol.*, 2017, **246**, p 276-284
- X. Zhao, B. Wang, D. Sun, C. Li, L. Han, and J. Gu, Effect of Pre-existing VC Carbides on Nitriding and Wear Behavior of Hot-Work Die Steel, *Appl. Surf. Sci.*, 2019, **486**, p 179-186
- J.Z. Lu, J. Cao, H.F. Lu, L.Y. Zhang, and K.Y. Luo, Wear Properties and Microstructural Analyses of Fe-Based Coatings with Various WC Contents on H13 Die Steel by Laser Cladding, *Surf. Coat. Technol.*, 2019, **369**, p 228-237
- S.L. Wang, Z.Y. Zhang, Y.B. Gong, and G.M. Nie, Microstructures and Corrosion Resistance of Fe-Based Amorphous/Nanocrystalline Coating Fabricated by Laser Cladding, *J. Alloys Compd.*, 2017, **728**, p 1116-1123
- Y. Lu, G. Huang, Y. Wang, H. Li, Z. Qin, and X. Lu, Crack-Free Fe-Based Amorphous Coating Synthesized by Laser Cladding, *Mater. Lett.*, 2018, **210**, p 46-50
- H. Zong, C. Geng, C. Kang, G. Cao, L. Bian, L. Li, B. Zhang, and M. Li, Excellent Glass Forming Ability and Plasticity in High Entropy Zr₂₀Ti₂₀Hf₂₀M₂₀Be₂₀ (M = Cu, Ni, Co) Alloys, *Results Phys.*, 2018, **8**, p 253-256
- P. Jinhong, H. Xiancong, and W. Zhangzhong, Preparation of High Entropy Alloy Cu₂₉Zr₃₂Ti₁₅Al₅Ni₁₉ with High Glass Forming Ability, *Rare Metal. Mater. Eng.*, 2017, **46**(7), p 1810-1814
- J. Kim, H.S. Oh, J. Kim, C.W. Ryu, G.W. Lee, H.J. Chang, and E.S. Park, Utilization of High Entropy Alloy Characteristics in Er-Gd-Y-Al-Co High Entropy Bulk Metallic Glass, *Acta Mater.*, 2018, **155**, p 350-361
- Y.Y. Zhao, Y.X. Ye, C.Z. Liu, R. Feng, K.F. Yao, and T.G. Nieh, Tribological Behavior of an Amorphous Zr₂₀Ti₂₀Cu₂₀-Ni₂₀Be₂₀ High-Entropy Alloy Studied Using a Nanoscratch Technique, *Intermetallics*, 2019, **113**, p 106561
- Z. Cai, Y. Wang, X. Cui, G. Jin, Y. Li, Z. Liu, and M. Dong, Design and Microstructure Characterization of FeCoNiAlCu High-Entropy Alloy Coating by Plasma Cladding: In Comparison with Thermodynamic Calculation, *Surf. Coat. Technol.*, 2017, **330**, p 163-169
- L. Liu, J.B. Zhu, C. Hou, J.C. Li, and Q. Jiang, Dense and Smooth Amorphous Films of Multicomponent FeCoNiCuVZrAl High-Entropy Alloy Deposited by Direct Current Magnetron Sputtering, *Mater. Des.*, 2013, **46**, p 675-679
- C. Wang, J. Yu, Y. Zhang, and Y. Yu, Phase Evolution and Solidification Cracking Sensibility in Laser Remelting Treatment of the Plasma-Sprayed CrMnFeCoNi High Entropy Alloy Coating, *Mater. Des.*, 2019, **182**, p 108040
- Y. Guo and Q. Liu, MoFeCrTiWAlNb Refractory High-Entropy Alloy Coating Fabricated by Rectangular-Spot Laser Cladding, *Intermetallics*, 2018, **102**, p 78-87
- Y.F. Juan, J. Li, Y.Q. Jiang, W.L. Jia, and Z.J. Lu, Modified Criteria for Phase Prediction in the Multi-Component Laser-Clad Coatings and Investigations into Microstructural Evolution/Wear Resistance of FeCrCoNiAlMox Laser-Clad Coatings, *Appl. Surf. Sci.*, 2019, **465**, p 700-714
- L. Jiang, W. Wu, Z. Cao, D. Deng, and T. Li, Microstructure Evolution and Wear Behavior of the Laser Cladded CoFeNi₂V_{0.5}Nb_{0.75} and CoFeNi₂V_{0.5}Nb High-Entropy Alloy Coatings, *J. Therm. Spray Technol.*, 2016, **25**(4), p 806-814
- C.L. Wu, S. Zhang, C.H. Zhang, H. Zhang, and S.Y. Dong, Phase Evolution and Properties in Laser Surface Alloying of FeCoCrAlCuNiX High-Entropy Alloy on Copper Substrate, *Surf. Coat. Technol.*, 2017, **315**, p 368-376
- Y.Q. Jiang, J. Li, Y.F. Juan, Z.J. Lu, and W.L. Jia, Evolution in Microstructure and Corrosion Behavior of AlCoCrXFeNi High-Entropy Alloys Coatings Fabricated by Laser Cladding, *J. Alloy Compd.*, 2019, **775**, p 1-14
- Y. Guo, X. Shang, and Q. Liu, Microstructure and Properties of In-Situ TiN Reinforced Laser Cladding CoCr₂FeNiTiX High-Entropy Alloy Composite Coatings, *Surf. Coat. Technol.*, 2018, **344**, p 353-358
- F.Y. Shu, S. Liu, H.Y. Zhao, W.X. He, S.H. Sui, J. Zhang, P. He, and B.S. Xu, Structure and High-Temperature Property of Amorphous Composite Coating Synthesized by Laser Cladding FeCrCoNiSiB High-Entropy Alloy Powder, *J. Alloys Compd.*, 2018, **731**, p 662-666
- P. Schoderböck, Investigation of Complex Residual Stress States in the Near-Surface Region: Evaluation of the Complete Stress Tensor by X-Ray Diffraction Pattern Decomposition, *Appl. Surf. Sci.*, 2019, **466**, p 151-164
- X. Gao, X. Lin, J. Yu, Y. Li, Y. Hu, W. Fan, S. Shi, and W. Huang, Selective Laser Melting (SLM) of In-Situ Beta Phase Reinforced Ti/Zr-Based Bulk Metallic Glass Matrix Composite, *Scr. Mater.*, 2019, **171**, p 21-25
- L. Yang, T. Ge, G.Q. Guo, C.L. Huang, X.F. Meng, S.H. Wei, D. Chen, and L.Y. Chen, Atomic and Cluster Level Dense Packing Contributes to the High Glass-Forming Ability in Metallic Glasses, *Intermetallics*, 2013, **34**, p 106-111
- B. Fultz, Vibrational Thermodynamics of Materials, *Prog. Mater. Sci.*, 2010, **55**(4), p 247-352
- Z.J. Yan, J.F. Li, S.R. He, and Y.H. Zhou, Evaluation of the Optimum Solute Concentration for Good Glass Forming Ability in Multicomponent Metallic Glasses, *Mater. Res. Bull.*, 2003, **38**(4), p 681-689
- F. Shu, B. Yang, S. Dong, H. Zhao, B. Xu, F. Xu, B. Liu, P. He, and J. Feng, Effects of Fe-to-Co Ratio on Microstructure and Mechanical Properties of Laser Cladded FeCoCrBNiSi High-Entropy Alloy Coatings, *Appl. Surf. Sci.*, 2018, **450**, p 538-544
- F. Shu, B. Zhang, T. Liu, S. Sui, Y. Liu, P. He, B. Liu, and B. Xu, Effects of Laser Power on Microstructure and Properties of Laser Cladded CoCrBFeNiSi High-Entropy Alloy Amorphous Coatings, *Surf. Coat. Technol.*, 2019, **358**, p 667-675

Publisher's Note Springer Nature remains neutral with regard to jurisdictional claims in published maps and institutional affiliations.